NONLINEAR PROJECTILE ATTITUDE ESTIMATION WITH MAGNETOMETERS AND ANGULAR RATE SENSORS

by

Michael J. Wilson

A thesis submitted to the Faculty of the University of Delaware in partial fulfillment of the requirements for the degree of Master of Electrical and Computer Engineering

Summer 2006

UMI Number: 1435820

UMI Microform 1435820

ProQuest Information and Learning Company
300 North Zeeb Road
P.O. Box 1346
Ann Arbor, MI 48106-1346

NONLINEAR PROJECTILE ATTITUDE ESTIMATION WITH MAGNETOMETERS AND ANGULAR RATE SENSORS

by

Michael J. Wilson

Approved: ______________________________

Gonzalo R. Arce, Ph.D.
Professor in charge of thesis on behalf of the Advisory Committee

Approved: ______________________________

Gonzalo R. Arce, Ph.D.
Chair of the Department of Electrical and Computer Engineering

Approved: ______________________________

Eric Kaler, Ph.D.
Dean of the College of Engineering

Approved: ______________________________

Daniel Rich, Ph.D.
Provost

ACKNOWLEDGMENTS

I would like to thank my beautiful wife, Sarah, for her loving support in my pursuit of this research, my advisor, Dr. Gonzalo Arce, for this opportunity and his guidance, and my colleagues at the US Army Research Laboratory, especially, Dave Lyon, Dave Hepner, and Tom Harkins, for their support and technical advice.

TABLE OF CONTENTS

LIST OF TABLES

LIST OF FIGURES

ABSTRACT

Recent advances in low cost sensor technologies and nonlinear estimation techniques are applicable to the navigation of gun-launched projectiles. A method for attitude (i.e. angular orientation) estimation is presented that uses magnetometers aided by angular rate sensors. Nonlinear state estimators provide the filtering mechanisms to combine the measurements based on their levels of accuracy. Results are presented using the extended Kalman filter (EKF) and the unscented Kalman filter (UKF), and the UFK is shown to outperform the EKF. The proposed method is demonstrated to provide a full attitude solution while satisfying the stringent requirements of gun-launched projectiles.

Chapter 1

INTRODUCTION

Over the years, the guidance, navigation, and control (GNC) of munitions has advanced considerably due to the introduction of high accuracy navigation devices such as GPS and semi-active laser seekers. The GNC for a missile, that is a rocket propelled munition, is quite mature, and several books currently exist that describe high accuracy navigation and the design of the guidance and control systems for missiles [1,2,3]. However, the GNC of a projectile, that is a gun-launched munition, is far from mature. The challenges of extremely high accelerations due to gun-launch and the unique dynamics of flight have rendered much of the missile GNC technologies inapplicable to projectiles, especially when it comes to sensors. Recent advances in micro-electrical mechanical systems (MEMS) have produced sensors that function onboard projectiles. However, their nonlinearities and inaccuracies present new challenges for the navigation problem.

Unlike a rocket, a projectile is a fairly accurate open-loop system. That is, projectiles can attain an acceptable level of accuracy system over long distances without any guidance. Specifically, artillery systems are accurate to about 100 meters at a range of several kilometers. Improving the precision of an unguided artillery round is highly desirable for two primary reasons. First, with the use of higher precision rounds, less rounds are required to destroy the target. Not only does improved precision provide a tactical advantage, but also minimizes the amount of rounds that must be carried. Second, a more accurate system minimizes collateral damage. This has become significantly relevant in the current conflicts where the risk of collateral damage prohibits the use of long range systems.

Despite the enormous gains of higher precision, GNC systems for projectiles must satisfy some steep requirements in order to be of any practical use. GNC components must survive gun launch and have a form factor small enough to fit in the available space inside a projectile. These two essential requirements are capable of being met by current technology. Gun hardened munition components have been extensively developed. And, miniaturization of electronics is a goal shared by several markets. Cost is by far the most important requirement driving the design of projectile GNC systems. Most "dumb" bullets cost only a few hundred dollars each. Therefore, million dollar guidance systems for these rounds are unrealistic.

High accuracy missile navigation systems typically do not satisfy these requirements. To achieve a high accuracy level with inaccurate sensors, robust estimation techniques are required. However, sensors well suited for projectile navigation such as magnetometers have outputs that are nonlinearly related to the attitude (i.e. angular orientation) states. Therefore, traditional linear filtering techniques are inapplicable and nonlinear techniques must be used.

Magnetometers have been shown to satisfy the above requirements and provide a measurement of attitude information onboard projectiles [4]. The magnetic field vector can be matched in both the earth-fixed and body-fixed coordinate systems, thus providing information about the rotation between the two. The problem of solving for the attitude of a rotating body by matching two or more non-zero, non-collinear vectors in multiple coordinate frames was first published by Wabha in 1965 [5]. (Two vector matches are required for a complete attitude solution.) Since then, several methods have been proposed to solve the vector-matching problem (for examples, see references [6,7,8]). Santoni and Bolotti devised an attitude determination system using magnetometers and solar panels [9]. These approaches were created for satellite applications when two or more vectors were known in the navigation and body frames. Psiaki [10] and Michalareas et al. [11] have spacecraft attitude determination systems that use only magnetometers. However, the filters used in these systems require the torques to be known and therefore do not apply to projectiles.

The proposed method relies on nonlinear estimation techniques and a coordinate system transformation that allows angular rate sensors to naturally assist the attitude determination while keeping the system heavily dependent on magnetometers. The angular rate sensors provide additional attitude measurements, but are in general much less accurate than magnetometers. The filtering approach allows the accuracy of the sensor to influence the reliance of the state estimate on that sensor. Therefore, the states are estimated in a more robust fashion then simply by solving the equations.

This thesis is organized as follows: Chapter 2 presents the background material in sensor models and flight parameters. Chapter 3 describes the nonlinear filtering techniques that will be used. Chapter 4 describes the desired states to be estimated in detail and provides the equations used in the filter for state propagation and the measurements. Chapter 5 shows the results of applying the nonlinear estimation techniques with a real ballistic trajectory. Chapter 6 concludes the thesis.

Chapter 2

SENSOR MODELS AND FLIGHT PARAMETERS

Coordinate Systems and Flight Parameters

Denote the earth-fixed Cartesian frame as $\{X,Y,Z\}$. This system is usually chosen to be the north, east, down system: the X axis points northward in a local plane tangential to the earth's surface. Likewise, the Y axis points eastward. The right-handed system is completed with the Z axis pointing toward the center of the earth. Denote the body-fixed frame $\{x,y,z\}$ with the x axis along the body's axis of symmetry or spin axis pointed in the direction of motion and the y and z axes oriented to complete the orthogonal right-handed system. Figure 1 shows both coordinate systems and the Euler angle relations between them.

The earth-fixed and body-fixed frames are related by an Euler rotation sequence beginning with first rotating the earth-fixed frame about the Z axis through the yaw angle ψ. The system is then rotated about the new Y axis through the pitch angle θ. Finally, the system is rotated about the new X axis through the roll angle ϕ. The two systems are related by the direction cosine matrix (DCM), $\mathbf{L}_{be}(\boldsymbol{\varepsilon})$, parameterized by the three Euler angles, $\boldsymbol{\varepsilon}=(\psi,\theta,\phi)^T$, with the subscript denoting earth-fixed to body-fixed. The form of this DCM is

$$\mathbf{L}_{be}(\boldsymbol{\varepsilon})=\begin{pmatrix} c_\psi c_\theta & s_\psi c_\theta & -s_\theta \\ c_\psi s_\theta s_\phi - s_\psi c_\phi & s_\psi s_\theta s_\phi + c_\psi c_\phi & c_\theta s_\phi \\ c_\psi s_\theta c_\phi + s_\psi s_\phi & s_\psi s_\theta c_\phi - c_\psi s_\phi & c_\theta c_\phi \end{pmatrix}, \tag{1.1}$$

where $c_\bullet$ is $\cos(\bullet)$, and $s_\bullet$ is $\sin(\bullet)$. Let the angular velocity vector of the projectile-fixed system with respect to the earth-fixed system be denoted as $\boldsymbol{\omega} = (p,q,r)^T$, in which p is the angular velocity of the y and z axes about the x axis; q is the angular velocity of the z and x axes about the y axis; r is the angular velocity of the x and y axes about the z axis. The derivatives of the Euler angles are related to the angular rates by

$$\begin{pmatrix} \dot{\phi} \\ \dot{\theta} \\ \dot{\psi} \end{pmatrix} = \begin{pmatrix} 1 & s_\phi t_\theta & c_\phi t_\theta \\ 0 & c_\phi & -s_\phi \\ 0 & s_\phi / c_\theta & c_\phi / c_\theta \end{pmatrix} \begin{pmatrix} p \\ q \\ r \end{pmatrix}, \tag{1.2}$$

where $t_\bullet$ is $\tan(\bullet)$.

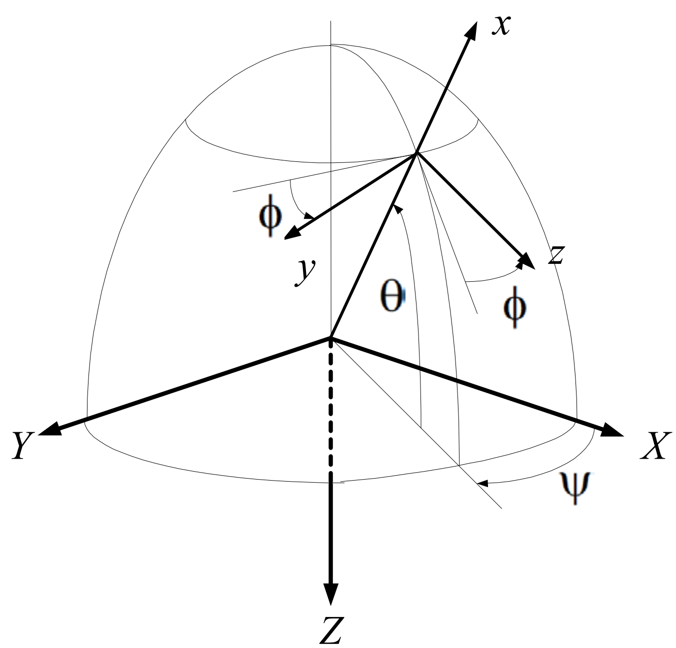

Figure 1: Navigation and Body-Fixed Frames

Sensor Models

A magnetometer is a device that produces a voltage output proportional to the applied magnetic field in the direction of the magnetometer's sensitive axis. If the magnetometer's sensitive axis is given by the unit vector,

$$\mathbf{v} = (v_1, v_2, v_3)^T, \tag{1.3}$$

and the local magnetic field applied to the magnetometer is

$$\mathbf{B} = (B_1, B_2, B_3)^T, \tag{1.4}$$

then, for a perfect sensor, the magnetometer output, m, is essentially the inner product (dot product) of $\mathbf{v}$ and $\mathbf{B}$:

$$m_{ideal} = \langle \mathbf{v}, \mathbf{B} \rangle. \tag{1.5}$$

Of course, the magnetometer output is actually scaled and shifted by analog circuitry. Therefore, the actual sample taken from a scaled and shifted magnetometer voltage output on an ADC is modeled as

$$m_{actual} = s \langle \mathbf{v}, \mathbf{B} \rangle + b \tag{1.6}$$

where s is the scale factor, b is the bias offset, and the effects of quantization introduced by the ADC are ignored.

Three magnetometers whose sensitive axes are linearly independent (i.e. not any two in the same direction) provide outputs that span three-dimensional space. Thus, using a 3-axis magnetometer or magnetometer triad provides the ability to measure completely the applied magnetic field in any direction. Consider three magnetometers whose outputs are

$$m_i = s_i \langle \mathbf{v}_i, \mathbf{B} \rangle + b_i \tag{1.7}$$

$$m_j = s_j \langle \mathbf{v}_j, \mathbf{B} \rangle + b_j \tag{1.8}$$

$$m_k = s_k \langle \mathbf{v}_k, \mathbf{B} \rangle + b_k \tag{1.9}$$

Equations (1.7) through (1.9) can be rewritten in matrix form by defining the following:

$$\mathbf{m} = (m_i, m_j, m_k)^T \tag{1.10}$$

$$\mathbf{b} = (b_i, b_j, b_k)^T \tag{1.11}$$

$$\mathbf{D} = \begin{pmatrix} d_{i1} & d_{i2} & d_{i3} \\ d_{j1} & d_{j2} & d_{j3} \\ d_{k1} & d_{k2} & d_{k3} \end{pmatrix} \tag{1.12}$$

and $d_{tu} = s_t v_{tu}$ where $t = \{i, j, k\}$ and $u = \{1,2,3\}$. The matrix equation is therefore

$$\mathbf{m} = \mathbf{DB} + \mathbf{b} \tag{1.13}$$

that when solved for $\mathbf{B}$ yields

$$\mathbf{B} = \mathbf{D}^{-1}(\mathbf{m} - \mathbf{b})\,. \tag{1.14}$$

Equation (1.14) represents the value of the applied magnetic field in the body-fixed coordinate system as a function of the magnetometer outputs and the calibration parameters $\mathbf{D}$ and $\mathbf{b}$. Therefore, there are 12 calibration parameters that must be determined in order to account for bias, scale, and alignment of a 3-axis magnetometer. See [12] for details on determining these parameters. The more complex models and calibrations required to account for material effects and electromagnetic interference are beyond the scope of this thesis.

The SNR for a magnetometer is usually very high; however, some amount of random noise is always present. Therefore, the final model considered for a magnetometer is

$$\mathbf{m} = \mathbf{D}_m\mathbf{B} + \mathbf{b}_m + \mathbf{v} \tag{1.15}$$

where $\mathbf{v}$ is zero mean Gaussian distributed with covariance matrix $\mathbf{R}_{vv}$.

Angular rate sensors are modeled in the same manner as magnetometers. Essentially, the projectile's angular rate vector is projected onto the sensor axes. A three-axis sensor is modeled as

$$\mathbf{r} = \mathbf{D}_r \boldsymbol{\omega} + \mathbf{b}_m + \boldsymbol{\eta} \tag{1.16}$$

where $\boldsymbol{\eta}$ is zero mean Gaussian distributed with variance $\mathbf{R}_{\eta\eta}$.

Chapter 3

NONLINEAR STATE ESTIMATION

Problem Definition

Let n be a discrete-time index and $\mathbf{x}(n)$ be a state vector $(N_x \times 1)$ that evolves in time according to

$$\mathbf{x}(n) = \mathbf{f}\left[\mathbf{x}(n-1), \mathbf{w}(n-1)\right], \tag{3.1}$$

where $\mathbf{w}(n)$ is the process noise sequence. Also let $\mathbf{y}(n)$ be a vector $(N_y \times 1)$ of measurements or observations that are related to the state vector by

$$\mathbf{y}(n) = \mathbf{h}\left[\mathbf{x}(n), \mathbf{v}(n)\right], \tag{3.2}$$

where $\mathbf{v}(n)$ is the measurement noise. In general, optimal estimates of $\mathbf{x}(n)$ could be found using the conditional probability density function (pdf), $p\left[\mathbf{x}(n) \,|\, Y_n\right]$, where Y_n is the set of all measurements up to and including time n. However, closed form solutions for this pdf rarely exist, and suboptimal methods must be considered.

It is well known that when $\mathbf{f}$ and $\mathbf{h}$ are linear and $\mathbf{w}$ and $\mathbf{v}$ are Gaussian distributed, the Kalman filter is the optimal solution in the mean square error sense. When $\mathbf{f}$ and $\mathbf{h}$ are nonlinear, there are several filtering methods available, the simplest being to linearize $\mathbf{f}$ and $\mathbf{h}$ when required in the Kalman filter equations resulting in the extended Kalman filter (EKF). If the linearization is a poor approximation to the actual functions, an unscented Kalman filter (UKF) can be used. In what follows, $\hat{\mathbf{P}}$ is the covariance matrix of the state estimate and its recursive formulation is presented below. Both the EKF and UKF are recursive and begin with the initial conditions

$$\hat{\mathbf{x}}(0\,|\,0), \quad \hat{\mathbf{P}}(0\,|\,0)\,. \tag{3.3}$$

In what follows, the notation $x(n\,|\,m)$ means the value of x at time n given all the information up to and including time m. For a complete description of both nonlinear filters, see [13].

Extended Kalman Filter

In this method, a Kalman filter is implemented with linearizations of $\mathbf{f}$ and $\mathbf{h}$ where appropriate. Essentially, the functions are approximated with a first order Taylor series in the covariance propagation and measurement weighting. The two required Jacobians are defined as

$$\mathbf{F}(n-1) = \left\{\nabla_{\mathbf{x}(n-1)}\mathbf{f}^T[\mathbf{x}(n-1)]\right\}^T\Big|_{\mathbf{x}(n-1)=\hat{\mathbf{x}}(n-1|n-1)} \tag{3.4}$$

$$\mathbf{H}(n) = \left\{\nabla_{\mathbf{x}(n)}\mathbf{h}^T[\mathbf{x}(n)]\right\}^T\Big|_{\mathbf{x}(n)=\hat{\mathbf{x}}(n|n-1)} \tag{3.5}$$

where

$$\nabla_{\mathbf{x}(n)} = \begin{bmatrix} \dfrac{\partial}{\partial x_1(n)} & \cdots & \dfrac{\partial}{\partial x_{N_x}(n)} \end{bmatrix}^T . \tag{3.6}$$

At each time step, the state vector and its covariance is predicted (propagated) forward using

$$\hat{\mathbf{x}}(n\,|\,n-1) = \mathbf{f}[\hat{\mathbf{x}}(n-1\,|\,n-1)] \tag{3.7}$$

$$\hat{\mathbf{P}}(n\,|\,n-1) = \mathbf{F}(n-1)\hat{\mathbf{P}}(n-1\,|\,n-1)\mathbf{F}^T(n-1) + \mathbf{R}_{ww}\,. \tag{3.8}$$

Next, the innovation is computed with its associated covariance as

$$\mathbf{e}(n) = \mathbf{y}(n) - \mathbf{H}[\hat{\mathbf{x}}(n\,|\,n-1)] \tag{3.9}$$

$$\mathbf{R}_{ee}(n) = \mathbf{H}[\hat{\mathbf{x}}(n\,|\,n-1)]\hat{\mathbf{P}}(n\,|\,n-1)\mathbf{H}^T[\hat{\mathbf{x}}(n\,|\,n-1)] + \mathbf{R}_{vv}\,. \tag{3.10}$$

The gain matrix is computed as

$$\mathbf{K}(n) = \hat{\mathbf{P}}(n\,|\,n-1)\mathbf{H}^T[\hat{\mathbf{x}}(n\,|\,n-1)]\mathbf{R}_{ee}^{-1}(n)\,. \tag{3.11}$$

Finally, the state estimate and its covariance is corrected using the measurements

$$\hat{\mathbf{x}}(n\,|\,n) = \hat{\mathbf{x}}(n\,|\,n-1) + \mathbf{K}(n)\mathbf{e}(n) \tag{3.12}$$

$$\hat{\mathbf{P}}(n \mid n) = \left\{\mathbf{I} - \mathbf{K}(n)\mathbf{H}[\hat{\mathbf{x}}(n \mid n-1)]\right\}\hat{\mathbf{P}}(n \mid n-1)\,. \tag{3.13}$$

Unscented Kalman Filter

The UKF relies on the principle that it is easier to approximate a pdf then an arbitrary nonlinear function [14]. Therefore, the UKF uses a set of weighted "sigma" points to estimate the states and covariances. At each step define the set of sigma points and associated weights as

$$\boldsymbol{\chi}_0 = \hat{\mathbf{x}}(n-1 \mid n-1), \quad W_0 = \frac{\kappa}{N_x + \kappa} \tag{3.14}$$

$$\begin{aligned} \boldsymbol{\chi}_{i/i+N_x} &= \hat{\mathbf{x}}(n-1 \mid n-1) \pm \left\{\sqrt{(N_x + \kappa)[\hat{\mathbf{P}}(n-1 \mid n-1) + \mathbf{R}_{ww}]}\right\}_i \\ W_{i/i+N_x} &= \frac{1}{2(N_x + \kappa)} \end{aligned}\,. \tag{3.15}$$

where κ is a tuning parameter and $\left\{\sqrt{\bullet}\right\}_i$ is the ith column of the matrix square root. Essentially, the sigma points are samples of the state space, one at the expected mean, and the others at fixed variances away from the mean. Each sigma point is then propagated forward, and the state prediction and covariance are formed as weighted sums,

$$\boldsymbol{\chi}_i(n \mid n-1) = \mathbf{f}[\boldsymbol{\chi}_i(n-1 \mid n-1)] \tag{3.16}$$

$$\hat{\mathbf{x}}(n \mid n-1) = \sum_{i=0}^{2N_x} W_i \boldsymbol{\chi}_i(n \mid n-1) \tag{3.17}$$

$$\hat{\mathbf{P}}(n \mid n-1) = \sum_{i=0}^{2N_x} W_i [\boldsymbol{\chi}_i(n \mid n-1) - \hat{\mathbf{x}}(n \mid n-1)][\boldsymbol{\chi}_i(n \mid n-1) - \hat{\mathbf{x}}(n \mid n-1)]^T\,. \tag{3.18}$$

By doing so, the effect of the nonlinearity on the state is approximated by the sigma points. Next, each sigma point is used to predict the measurements and the cross-covariance and covariance are calculated,

$$\boldsymbol{\xi}_i(n \mid n-1) = \mathbf{f}[\boldsymbol{\chi}_i(n \mid n-1)] \tag{3.19}$$

$$\hat{\mathbf{y}}(n|n-1) = \sum_{i=0}^{2N_x} W_i \boldsymbol{\xi}_i(n|n-1) \tag{3.20}$$

$$\mathbf{R}_{\hat{y}\hat{y}}(n|n-1) = \sum_{i=0}^{2N_x} W_i [\boldsymbol{\xi}_i(n|n-1) - \hat{\mathbf{y}}(n|n-1)][\boldsymbol{\xi}_i(n|n-1) - \hat{\mathbf{y}}(n|n-1)]^T \tag{3.21}$$

$$\mathbf{R}_{\hat{x}\hat{y}}(n|n-1) = \sum_{i=0}^{2N_x} W_i [\boldsymbol{\chi}_i(n|n-1) - \hat{\mathbf{x}}(n|n-1)][\boldsymbol{\xi}_i(n|n-1) - \hat{\mathbf{y}}(n|n-1)]^T . \tag{3.22}$$

The covariances then determine the gain, and the measurement update is computed as

$$\mathbf{K}(n) = \mathbf{R}_{\hat{x}\hat{y}}(n|n-1)\mathbf{R}_{\hat{y}\hat{y}}(n|n-1) \tag{3.23}$$

$$\hat{\mathbf{x}}(n|n) = \hat{\mathbf{x}}(n|n-1) + \mathbf{K}(n)[\mathbf{y}(n) - \hat{\mathbf{y}}(n|n-1)] \tag{3.24}$$

$$\hat{\mathbf{P}}(n|n) = \hat{\mathbf{P}}(n|n-1) - \mathbf{K}(n)\mathbf{R}_{\hat{y}\hat{y}}(n|n-1)\mathbf{K}^T(n) . \tag{3.25}$$

Chapter 4

STATE DYNAMICS AND MEASUREMENT MODELS

Magnetic Pitch and Roll Angles

A magnetic roll angle, ϕ_{mag}, is defined as the angle in the $j-k$ $(y-z)$ plane between the k-axis and the earth's magnetic field projected into the $j-k$ plane (see Figure 2). ϕ_{mag} can also be viewed as the third angle in an aerospace Euler sequence with an arbitrary yaw angle and a pitch angle

$$\theta_{mag} = \cos^{-1} B_i \,. \tag{4.1}$$

ϕ_{mag} can be estimated with uncalibrated radial magnetometers; however, the magnetometers must be gain matched and without bias. Fortunately, this can be achieved through processing of the radial magnetometers' sinusoidal output.

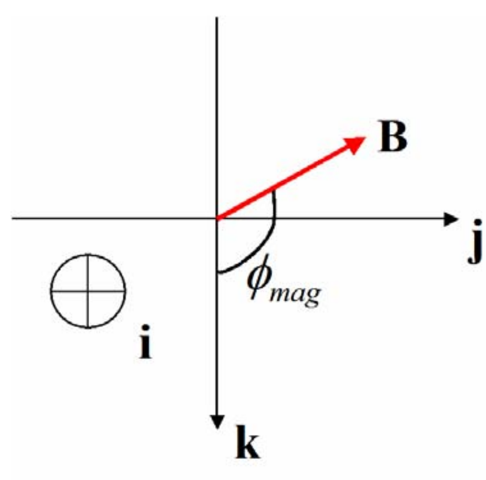

Figure 2: Magnetic roll angle

Figure 3 shows the output of radial magnetometers over a short period of time for a trajectory. Notice the sinusoidal output as a result of the projectile spin, and the two sensors are 90 degrees out of phase. Each sensor, in general, has a different scale factor and bias as demonstrated in the figure.

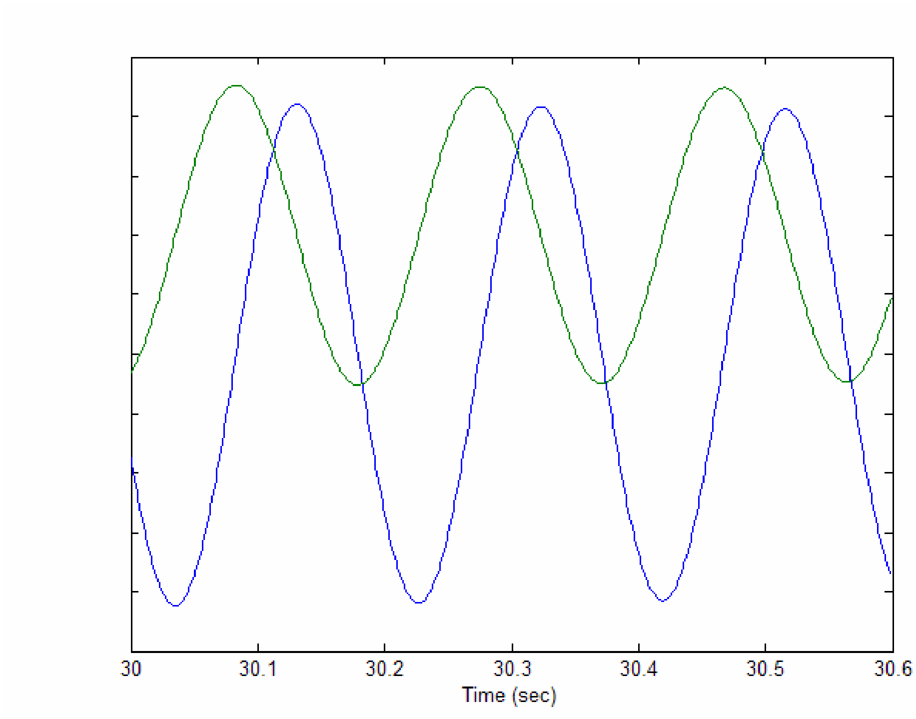

Figure 3: Radial magnetometer signals

Because of the geometry of the problem, the peak-to-peak amplitude of both sensors should be the same, and both sensors should oscillate about zero. Therefore, the bias from each sensor can be removed, and the resulting signals can be gain matched, resulting in the signals, m_j' and m_k', shown in Figure 4. Thus, ϕ_{mag} is estimated as

$$\hat{\phi}_{mag} = \tan^{-1}\left(\frac{m_j'}{m_k'}\right) \qquad (4.2)$$

This estimate could also be achieved via a phase lock loop (PLL) to track the phase of either m_j', m_k', or both.

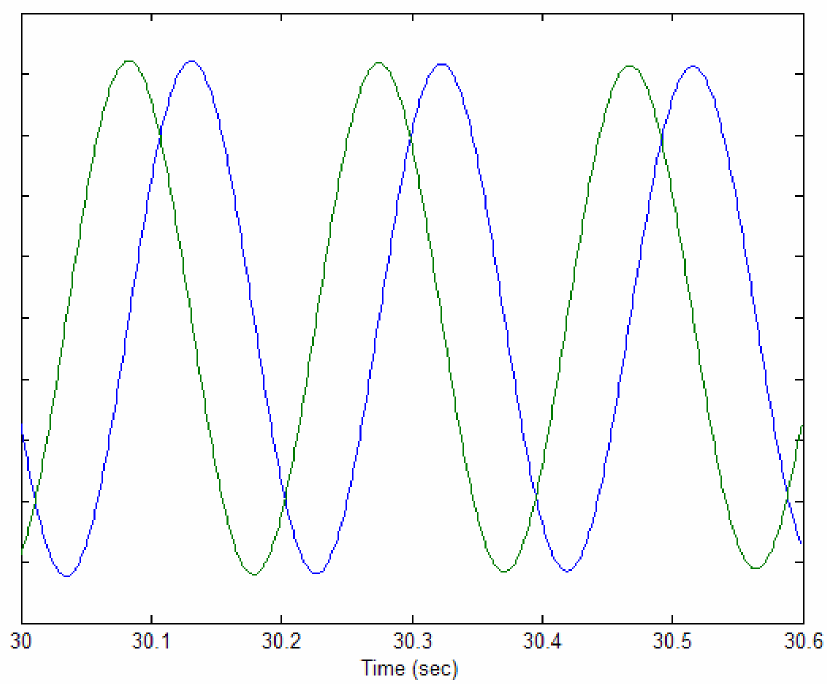

Figure 4: Radial magnetometers' output after gain matching and bias removal

For small yaw, the temporal derivative of the magnetic roll angle, $\dot{\phi}_{mag}$, can be estimated by the frequency of the sine waves generated by the radially oriented magnetometers. This is usually achieved by measuring the times between zero crossings or extrema points; however, any frequency estimation technique can be applied.

$\dot{\phi}_{mag}$ is related to other flight parameters of interest such as the spin rate, p, and the roll Euler angle in the aerospace sequence, ϕ. The derivatives of the Euler angles are related to the body-fixed angular rates as

$$\begin{pmatrix} \dot{\phi} \\ \dot{\theta} \\ \dot{\psi} \end{pmatrix} = \begin{pmatrix} 1 & s_\phi t_\theta & c_\phi t_\theta \\ 0 & c_\phi & -s_\phi \\ 0 & s_\phi / c_\theta & c_\phi / c_\theta \end{pmatrix} \begin{pmatrix} p \\ q \\ r \end{pmatrix} \tag{4.3}$$

The first line of (4.3) relates p to some ϕ in an Euler sequence. However, p is also a function of q, r, and θ. Therefore, a measurement of ϕ_{mag} or any other Euler sequence roll angle, is not a direct measurement of p but does have a strong functional dependence on the spin rate if it is high relative to the other angular rates. Inverting (4.3) yield p as a function of the Euler angle derivatives:

$$p = \dot{\phi} - \dot{\psi}\sin(\theta). \tag{4.4}$$

Using equation (4.4) to relate p to ϕ_{mag} yields

$$p = \dot{\phi}_{mag} - \dot{\psi}_{mag}\sin(\theta_{mag}). \tag{4.5}$$

in which θ_{mag} was defined in (4.1) and $\dot{\psi}_{mag}$ is the rate of rotation about the earth's magnetic field vector. Also, setting (4.4) (with the Euler sequence ϕ) and (4.5) equal to each other and solving for $\dot{\phi}$ yields

$$\dot{\phi} = \dot{\phi}_{mag} - \dot{\psi}_{mag}\sin(\theta_{mag}) + \dot{\psi}\sin(\theta) \tag{4.6}$$

Notice that ϕ_{mag} could deviate from ϕ because of projectile overturning causing a nonzero $\dot{\psi}_{mag}$. This effect is greatest when the spin axis of the projectile passes close to the earth's magnetic field vector when $\left|\sin(\theta_{mag})\right| \approx 1$. Also, disturbances such as wind and maneuvers create a nonzero $\dot{\psi}$, causing the same effect.

To demonstrate the deviation of the Euler roll angle and the magnetic roll angle, a gun-fixed navigation frame is considered as shown in Figure 5. Three simulations of the same trajectory were run with different magnetic field directions as indicated in Figure 5. The magnetic field vectors all lie in the X-Y plane. The spin axis of the projectile makes its closest approach (largest θ_{mag}) at the apogee. The closer the alignment of the magnetic field vector with the X-axis, the more severe the effect of overturning will be on the change in the difference between the roll angles.

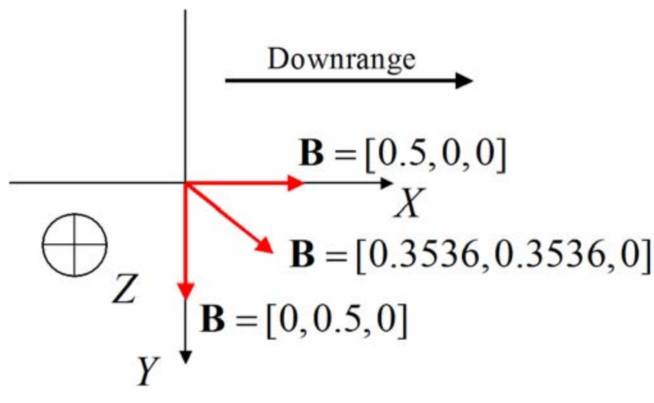

Figure 5: Sample magnetic field vector directions

This effect is demonstrated in Figure 6 where the difference in the Euler roll angle and the magnetic roll angle is plotted for the different magnetic field vectors. Because the values are angles, the maximum difference between them is 180 degrees. The flat portion of the curves indicates that roll angle derivatives are approximately equal. For the green curve ($\mathbf{B}$ aligned with the X-axis), the effect of overturning is dramatic but occurs over a short interval close to apogee. For the red curve ($\mathbf{B}$ 45 degrees off the X-axis), the effect is less severe but occurs over a wider time scale.

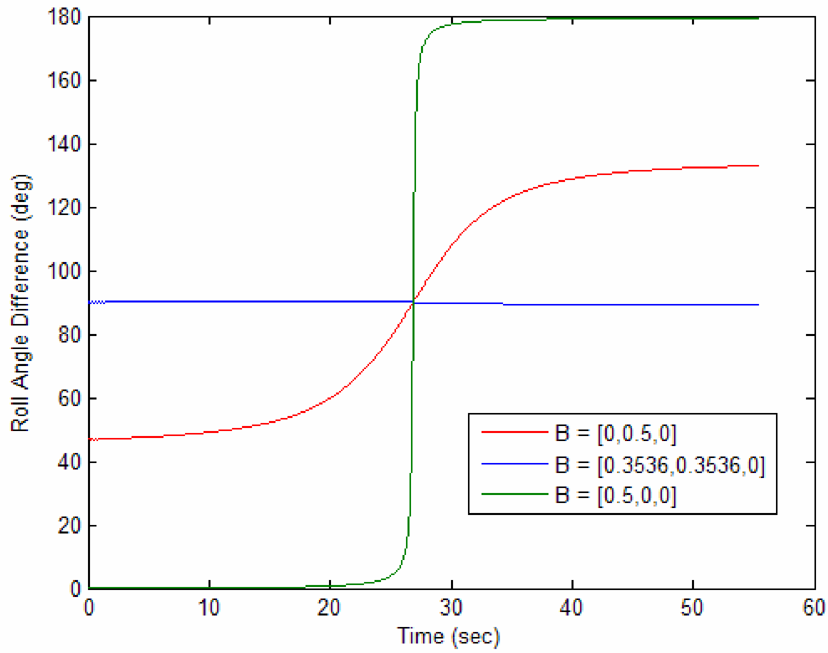

Figure 6: Roll angle difference for various magnetic field orientations

The Magnetic Coordinate Frame

The earth's magnetic field in the body frame is related to the earth-fixed frame as

$$\begin{pmatrix} B_x \\ B_y \\ B_z \end{pmatrix} = \begin{pmatrix} c_\psi c_\theta & s_\psi c_\theta & -s_\theta \\ c_\psi s_\theta s_\phi - s_\psi c_\phi & s_\psi s_\theta s_\phi + c_\psi c_\phi & c_\theta s_\phi \\ c_\psi s_\theta c_\phi + s_\psi s_\phi & s_\psi s_\theta c_\phi - c_\psi s_\phi & c_\theta c_\phi \end{pmatrix} \begin{pmatrix} B_X \\ B_Y \\ B_Z \end{pmatrix}. \tag{4.7}$$

Let $\{X_m, Y_m, Z_m\}$ be a "magnetic" frame where the Z_m axis is the earth's magnetic field vector. Also, for the remainder of this paper, assume the magnetic field vector is normalized to a unit vector. Equation (4.7) can be rewritten for the magnetic frame as

$$\begin{pmatrix} B_x \\ B_y \\ B_z \end{pmatrix} = \begin{pmatrix} c_\psi c_\theta & s_\psi c_\theta & -s_\theta \\ c_\psi s_\theta s_\phi - s_\psi c_\phi & s_\psi s_\theta s_\phi + c_\psi c_\phi & c_\theta s_\phi \\ c_\psi s_\theta c_\phi + s_\psi s_\phi & s_\psi s_\theta c_\phi - c_\psi s_\phi & c_\theta c_\phi \end{pmatrix} \begin{pmatrix} 0 \\ 0 \\ 1 \end{pmatrix} = \begin{pmatrix} -s_\theta \\ c_\theta s_\phi \\ c_\theta c_\phi \end{pmatrix}. \tag{4.8}$$

It is now obvious that the pitch and roll angles in (4.8) are the magnetic pitch and roll angles described by (4.1) and (4.2). In this magnetic coordinate system, the magnetometer measurements are simply related to the magnetic pitch and roll angles. This frame will be used as an intermediate frame to perform the estimation.

Dynamic Equations and States

Typical six degree-of-freedom (6DOF) aeroballistic trajectory simulations actually require twelve states. This is due to the fact that the angular motion of the projectile is nonlinearly coupled to the translational motion. Since the estimators considered here are for attitude, position or velocity sensors are not considered. Therefore, a simplified model of the dynamics is required that essentially will allow coupling between magnetometer and angular rate sensor data.

A geomagnetic sensor cannot distinguish a rotation about the earth's magnetic field vector, ψ_{mag}. θ_{mag} and ϕ_{mag} therefore provide a complete description of the information that is able to be sensed by a magnetometer. These two parameters are the states of the estimator, and are related to angular rate sensor outputs through (4.3). Discretizing with a simple Euler numerical integration technique yields the following state propagation equations

$$\begin{aligned} &\phi_{mag}(n+1) = \phi_{mag}(n) \\ &+\Delta t\left\{p(n) + \sin[\phi_{mag}(n)]\tan[\theta_{mag}(n)]q(n) + \cos[\phi_{mag}(n)]\tan[\theta_{mag}(n)]r(n)\right\} \end{aligned} \tag{4.9}$$

$$\theta_{mag}(n+1) = \theta_{mag}(n) + \Delta t\left\{\cos[\phi_{mag}(n)]q(n) - \sin[\phi_{mag}(n)]r(n)\right\} \tag{4.10}$$

where Δt is the time interval between each sample (assumed constant). In this manner, the angular rate sensors are used to smooth and correct the magnetometers.

Since ψ_{mag} is not observable through magnetometer measurements, it directly computed via numerical integration as

$$\psi_{mag}(n+1) = \psi_{mag}(n) + \Delta t \left\{ \frac{\sin[\phi_{mag}(n)]}{\cos[\theta_{mag}(n)]} q(n) + \frac{\cos[\phi_{mag}(n)]}{\cos[\theta_{mag}(n)]} r(n) \right\}. \qquad (4.11)$$

With all three magnetic Euler angles, the complete attitude is defined, and a coordinate transformation is executed into any earth-fixed, navigation frame of interest.

The angular rates themselves are too dependent on the translational motion to attempt to correct with an aerodynamic model. However, the general nonlinear estimation techniques presented here could be extended to include position and/or velocity sensors.

Measurements

The angular rate sensor measurements are "hard coupled" into the state propagation equations. From a filtering perspective, the magnetometers are the only measurements considered and are given by (4.8).

Chapter 5

RESULTS

A typical artillery projectile's trajectory with a low gun elevation (to minimize trajectory length) was simulated. Figure 7 plots the Euler angles, Figure 8 plots the angular rates, Figure 9 plots the magnetometer outputs, and Figure 10 is an alpha/beta plot that shows the motion of the tip of the nose of the projectile around its velocity vector. Note the typical symmetric epicyclic motion typical of spin stabilized projectiles. See [15] for a complete description of the motion of symmetric projectiles.

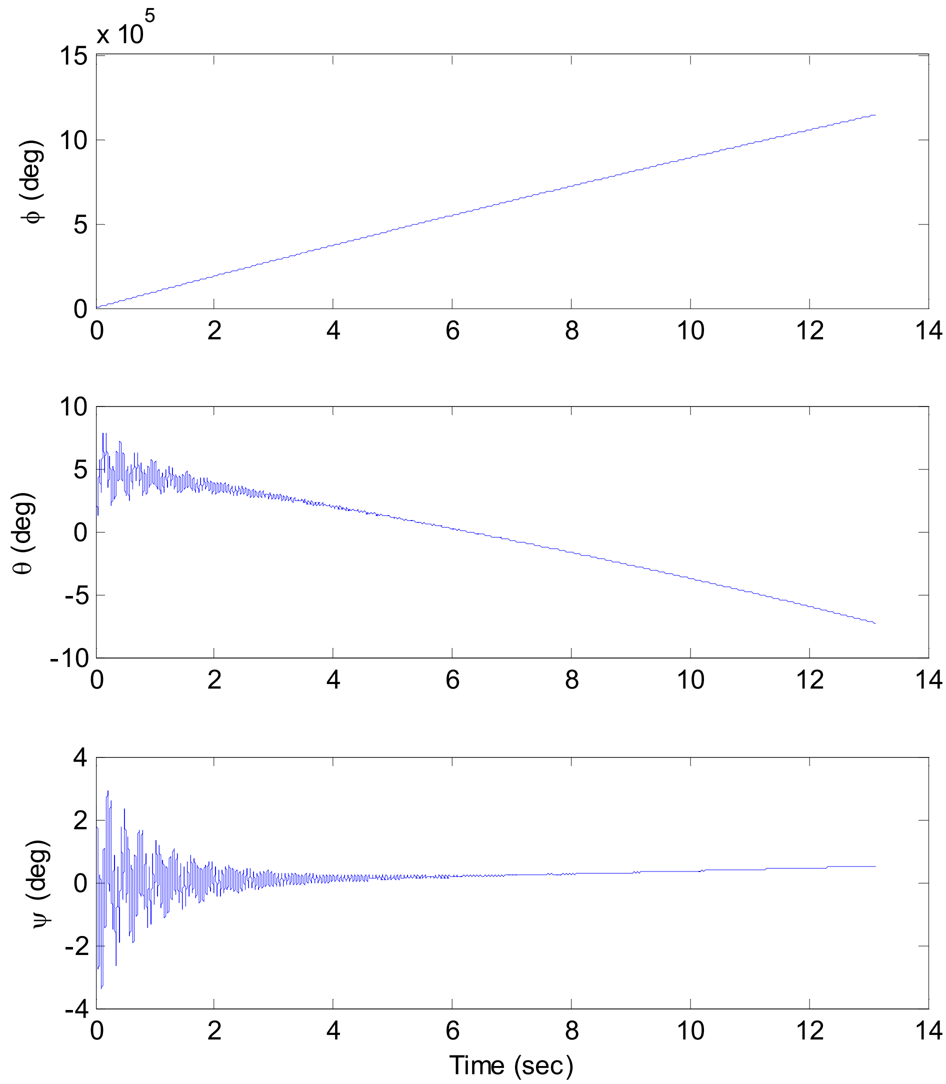

Figure 7: Euler angles

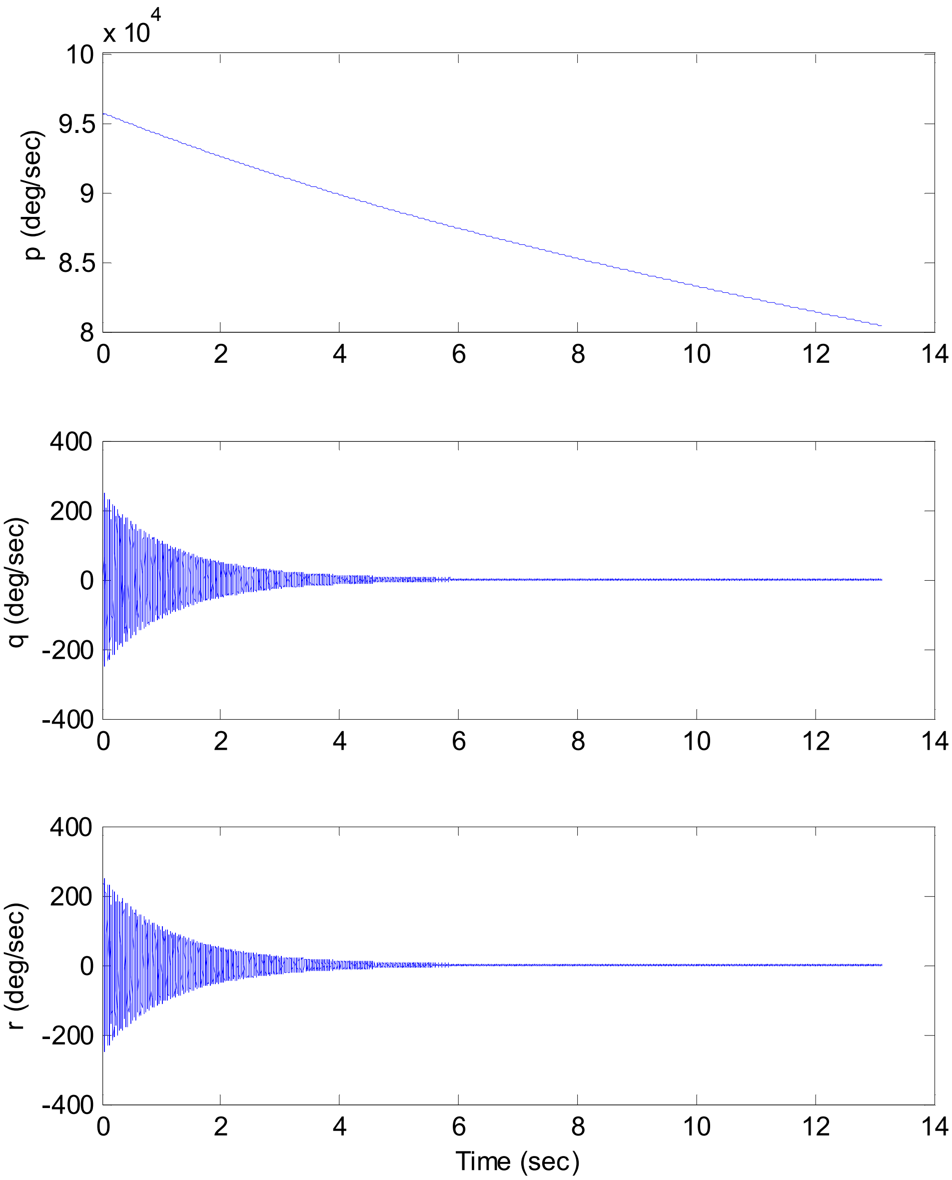

Figure 8: Angular rates

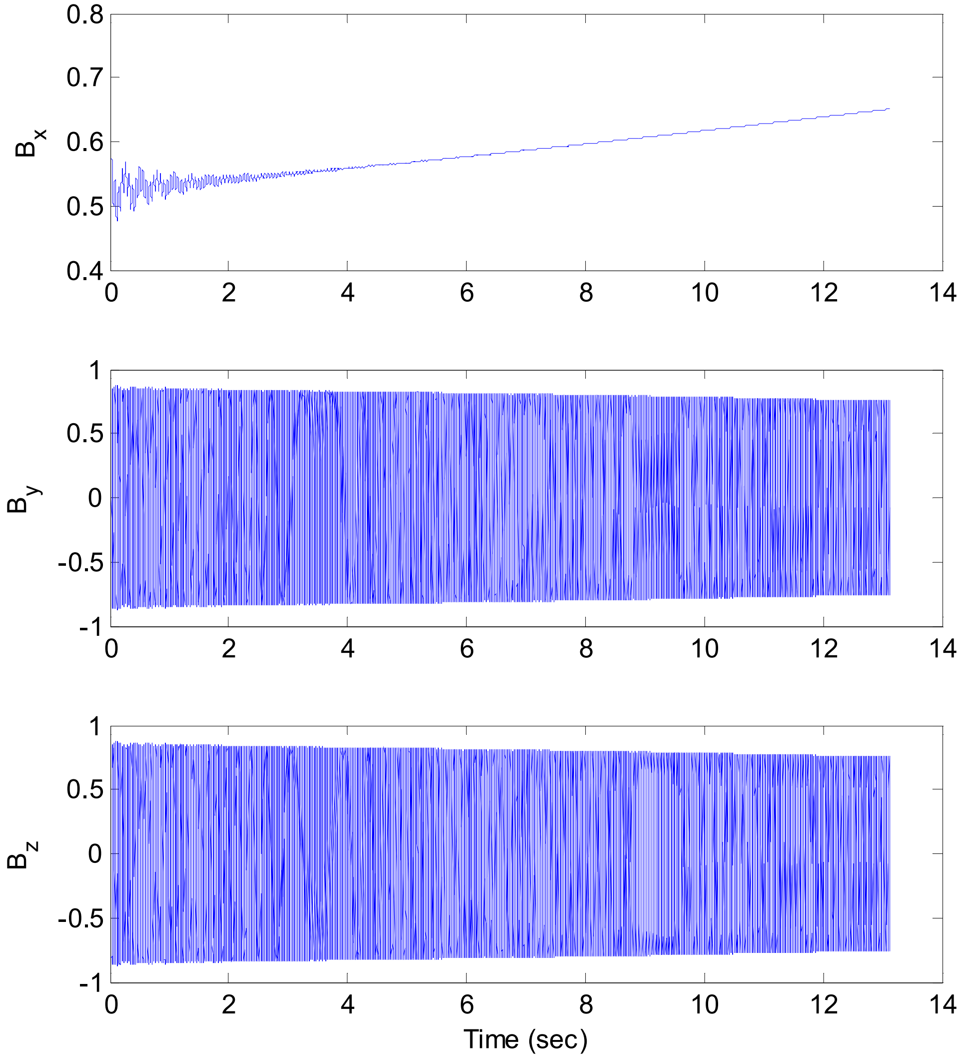

Figure 9: Magnetometer outputs

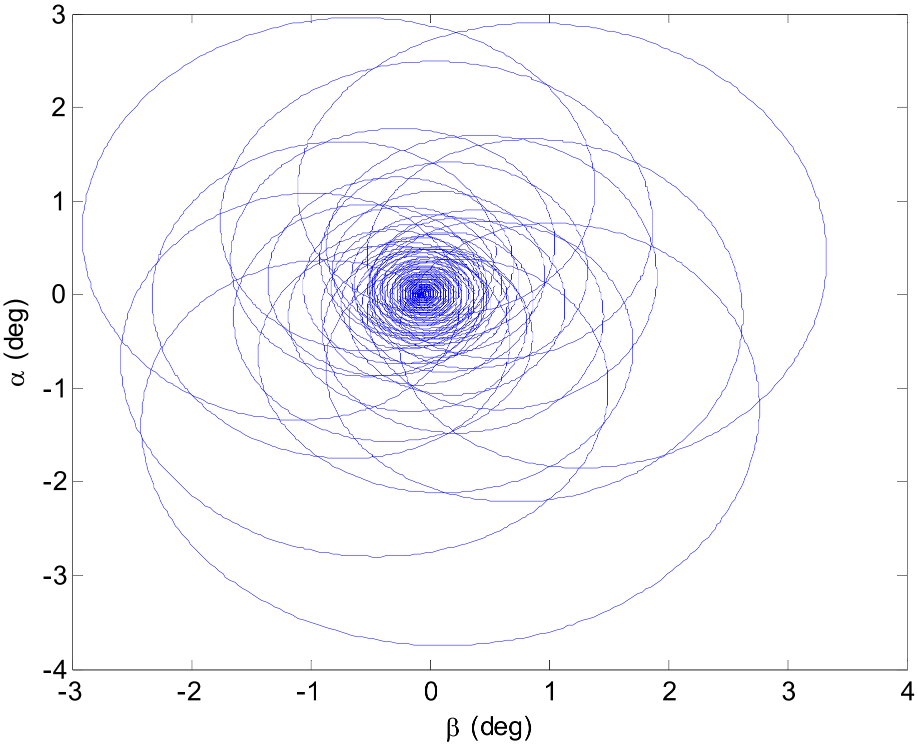

Figure 10: Angular motion of the tip of the projectile around the velocity vector

The filtering methods described in Chapter 3 where implemented using the equations, states, and measurements described in Chapter 4. In the simulations, $\mathbf{B}_e = (0.5774, 0.5774, 0.5774)^T$, $\mathbf{R}_{ww} = 10^{-8}\mathbf{I}$, $\mathbf{R}_{vv} = 10^{-6}\mathbf{I}$, which was also the covariance of the noise added to the simulated magnetometer outputs, and

$$\mathbf{R}_{\eta\eta} = \begin{pmatrix} 100 & 0 & 0 \\ 0 & 0.01 & 0 \\ 0 & 0 & 0.01 \end{pmatrix}$$

was the covariance of the noise added to the angular rate sensor outputs. The number of sigma points used in the UKF was $2N_x + 1 = 5$.

Figure 11 shows the first 2000 samples of the filtered magnetic pitch angle estimates compared with the actual values. The green curve is a direct computation of the pitch angle using the noisy magnetometer measurements. The plot demonstrates a significant improvement using the filtering techniques. It is not clear from the plot but shown in Table 1 that the UKF outperforms the EFK. The table shows the mean square error in the estimates of the magnetic pitch and roll angles over the entire trajectory. Figure 12 shows the entire trajectory estimates from the UKF for the navigation pitch and yaw angles. Since these angles are a function of all of the magnetic Euler angles, the drift in the magnetic yaw angle causes the estimate values to deviate from the actual later in the trajectory.

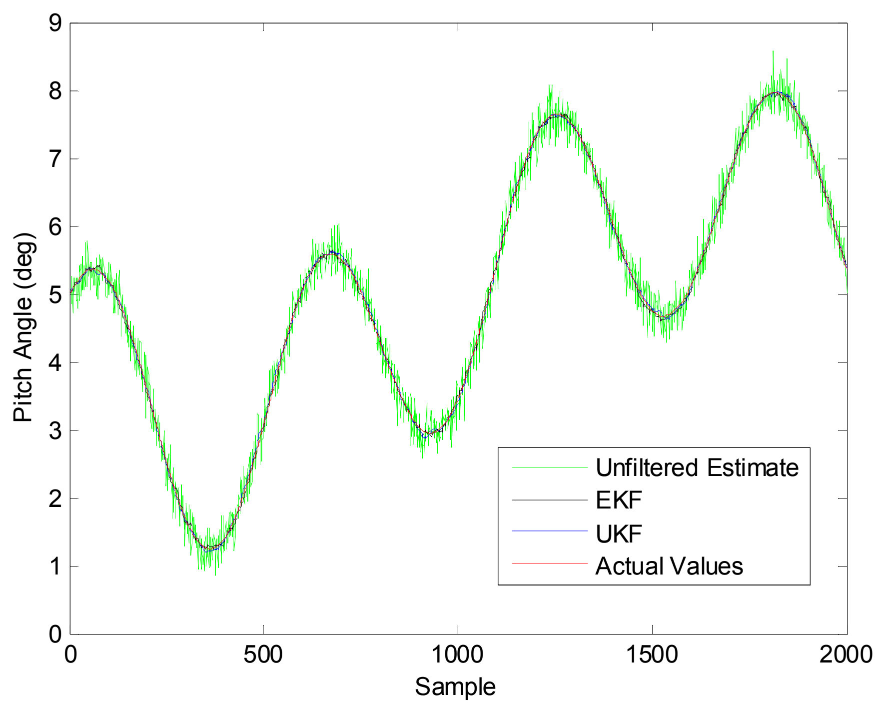

Figure 11: Magnetic pitch angle estimates from EKF, UKF, and direct computation

Table 1: Mean square errors for EKF and UKF

Mean Square Error	Magnetic Pitch Angle	Magnetic Roll Angle
EKF	5.3055e-7	4.9876e-6
UKF	3.6824e-7	1.8480e-6

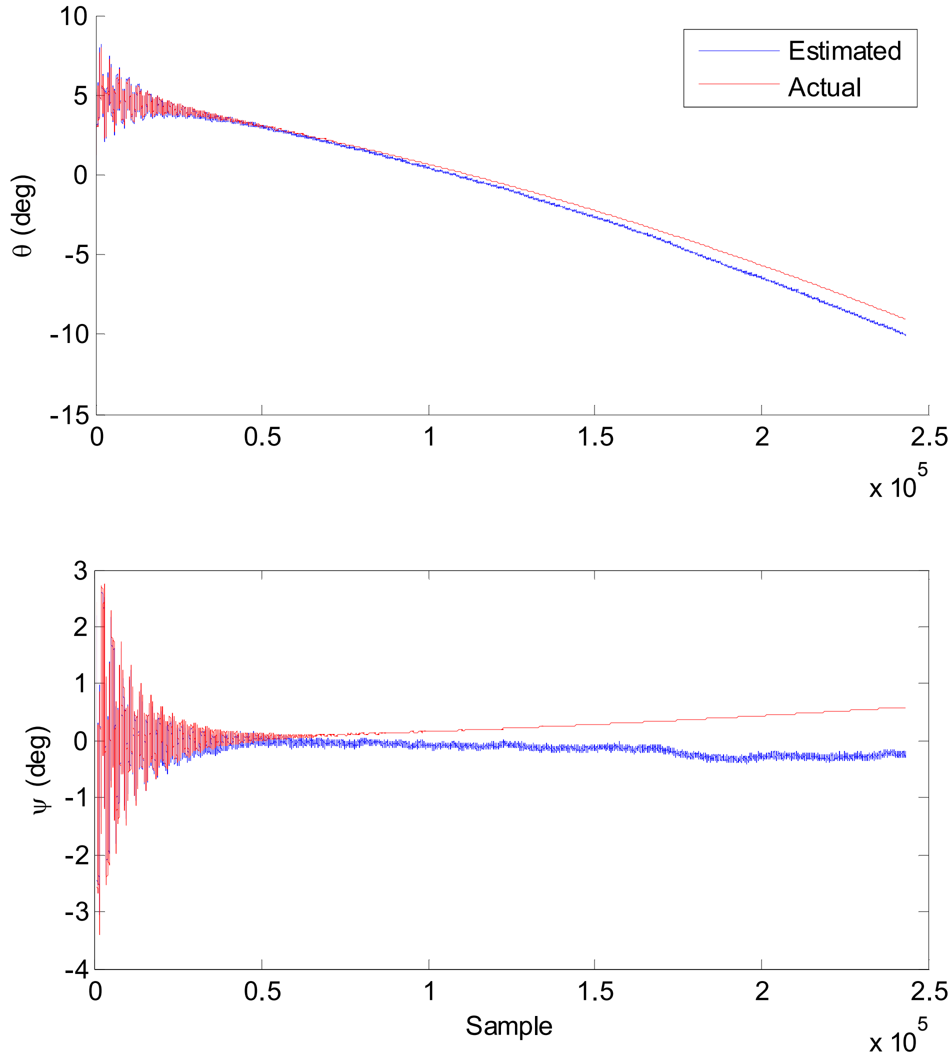

Figure 12: UKF estimates of pitch and yaw angles

Chapter 6

CONCLUSION

Nonlinear state estimation techniques have been applied to attitude estimation using magnetometers and angular rate sensors. The noise powers used in the simulations reflect the inaccuracies of currently available sensor systems that can be used with gun-launched projectiles. The filtering techniques were demonstrated to perform significantly better in estimating the states than direct calculation. The UKF, which approximates the pdfs instead of the nonlinear functions, showed superior performance over the EKF.

The filtering techniques considered are general and could be modified to include additional states and measurements. With the successful estimation of the attitude, position and velocity sensors such as a Global Positioning System (GPS) receiver could be included in the filter along with the additional states. The filter could also include a full model of the aerodynamic forces and moments and the controlled maneuvers.

REFERENCES

[1] A. Chatfield, *Fundamental of High Accuracy Inertial Navigation*, Progress in Astronautics and Aeronautics, Vol. 174, AIAA, Reston, VA, 1997.

[2] P. Zarchan, *Tactical and Strategic Missile Guidance*, Progress in Astronautics and Aeronautics, Vol. 174, AIAA, Reston, VA, 1997.

[3] G. Siouris, *Missile Guidance and Control Systems*, Springer, New York, NY, 2004.

[4] M. Wilson, "Attitude determination with magnetometers for gun-launched munitions, *US Army Research Laboratory*, Technical Report, ARL-TR-3209, August 2004.

[5] G. Wahba, "A least squares estimate of spacecraft attitude," *SIAM Review* 1965.

[6] I. Bar-Itzhack, Y. Oshman, "Attitude determination from vector observations: quaternion estimation," *IEEE Trans. Aerospace and Electronic Systems* January 1985, *AES-21*.

[7] I. Bar-Itzhack, M. Idan, "Recursive attitude determination from vector observations," *J. Guidance, Control, and Dynamics* March-April 1987.

[8] D. Mortari, “Euler-q algorithm for attitude determination from vector observations,” *J. Guidance, Control, and Dynamics* March-April 1998.

[9] F. Santoni, F. Bolotti, “Attitude determination of small spinning spacecraft using three-axis magnetometer and solar panel data,” *Proc. IEEE Aerospace* March 2000.

[10] M. Psiaki, “Global magnetometer-based spacecraft attitude and rate estimation,” *J. Guidance, Control, and Dynamics* March-April 2004.

[11] G. Michalareas, S. Gabriel, E. Rogers, “Spacecraft attitude estimation based on magnetometer measurements and the covariance intersection algorithm,” *Proc. IEEE Aerospace* March 2002.

[12] M. Wilson, A. Laroche, “Automatic three-axis magnetometer calibration,” *US Army Research Laboratory*, Technical Report, ARL-TR-3557, July 2005.

[13] J. Candy, *Model-Based Signal Processing*, IEEE, Wiley, Hoboken, NJ, 2006.

[14] S. Julier, J. Uhlmann, H. Durrant-Whyte, “A new approach for filtering in nonlinear systems,” Proc. Am. Contr. Conf., 1995.

[15] C. Murphy, “Free flight motion of symmetric missiles,” *US Ballistics Research Laboratory*, Technical Report, R1216, July 1963.